A year in the life of GW 170817: the rise and fall of a structured jet from a binary neutron star merger

E. Troja [1,2]⋆ H. van Eerten,[3] G. Ryan,[1] R. Ricci,[4] J. M. Burgess,[5,6] M. H. Wieringa,[7] L. Piro,[8] S. B. Cenko[2,1] and T. Sakamoto[9]

[1]*Department of Astronomy, University of Maryland, College Park, MD 20742-4111, USA*
[2]*Astrophysics Science Division, NASA Goddard Space Flight Center, 8800 Greenbelt Rd, Greenbelt, MD 20771, USA*
[3]*Department of Physics, University of Bath, Claverton Down, Bath BA2 7AY, UK*
[4]*INAF – Istituto di Radioastronomia, via Gobetti 101, I-40129 Bologna, Italy*
[5]*Max-Planck-Institut fur extraterrestrische Physik, Giessenbachstrasse 1, D-85748 Garching, Germany*
[6]*Excellence Cluster Universe, Technische Universität München, Boltzmannstraße 2, D-85748 Garching, Germany*
[7]*CSIRO Astronomy and Space Science, PO Box 76, Epping, NSW 1710, Australia*
[8]*INAF – Istituto di Astrofisica e Planetologia Spaziali, via Fosso del Cavaliere 100, I-00133 Rome, Italy*
[9]*Aoyama Gakuin University, 5-10-1 Fuchinobe, Chuoku, Sagamiharashi Kanagawa 252-5258, Japan*

ABSTRACT

We present the results of our year-long afterglow monitoring of GW 170817, the first binary neutron star merger detected by Advanced Laser Interferometer Gravitational-Wave Observatory (LIGO) and Advanced Virgo. New observations with the Australian Telescope Compact Array and the *Chandra X-ray Telescope* were used to constrain its late-time behaviour. The broad-band emission, from radio to X-rays, is well-described by a simple power-law spectrum with index $\beta \sim 0.585$ at all epochs. After an initial shallow rise $\propto t^{0.9}$, the afterglow displayed a smooth turnover, reaching a peak X-ray luminosity of $L_X \approx 5 \times 10^{39}$ erg s^{-1} at 160 d, and has now entered a phase of rapid decline, approximately $\propto t^{-2}$. The latest temporal trend challenges most models of choked jet/cocoon systems, and is instead consistent with the emergence of a relativistic structured jet seen at an angle of $\approx 22°$ from its axis. Within such model, the properties of the explosion (such as its blast wave energy $E_K \approx 2 \times 10^{50}$ erg, jet width $\theta_c \approx 4°$, and ambient density $n \approx 3 \times 10^{-3}$ cm^{-3}) fit well within the range of properties of cosmological short gamma-ray bursts.

Key words: acceleration of particles – gravitational waves – gamma-ray burst: general.

1 INTRODUCTION

On 2017 August 17 the Advanced Laser Interferometer Gravitational-Wave Observatory (LIGO) interferometers detected the first gravitational wave (GW) signal from a binary neutron star merger, GW 170817, followed 1.7 s later by a short-duration gamma-ray burst (GRB), GRB 170817A (Abbott et al. 2017b). Located in the elliptical galaxy NGC 4993 at a distance of ∼40 Mpc, GRB 170817A was an atypical subluminous explosion. An X-ray afterglow was detected 9 d after the merger (Troja et al. 2017). A second set of observations, performed ∼15 d post-merger, revealed that the emission was not fading, as standard gamma-ray burst (GRB) afterglows, but was instead rising at a slow rate (Haggard et al. 2017; Troja et al. 2017). The radio afterglow, detected at 16 d (Hallinan et al. 2017), continued to rise in brightness (Mooley

et al. 2018a), as later confirmed by X-ray and optical observations (D'Avanzo et al. 2018; Lyman et al. 2018; Margutti et al. 2018; Troja et al. 2018a).

The delayed afterglow onset and low luminosity of the gamma-ray signal could be explained if the jet was observed at an angle (off-axis) of ≈15°–30°. Although a standard uniform jet viewed off-axis could account for the early afterglow emission, Troja et al. (2017) and Kasliwal et al. (2017) noted that it could not account for the observed gamma-ray signal and proposed two alternative models: a structured jet, i.e. a jet with an *angular* profile of Lorentz factors and energy (see also Abbott et al. 2017b; Kathirgamaraju, Barniol Duran & Giannios 2018), and a mildly relativistic isotropic cocoon (see also Kasliwal et al. 2017; Lazzati et al. 2017). In the latter model, the jet may never emerge from the merger ejecta (choked jet).

The subsequent rebrightening ruled out both the uniform jet and the simple cocoon models, which predict a sharp afterglow rise. It was instead consistent with an off-axis structured jet

⋆ E-mail: eleonora@umd.edu

Table 1. Late-time X-ray and radio observations of GW 170817.

$T - T_0$ (d)	Facility	Exposure	β	Flux[a] (μJy)	Frequency (GHz)
267	ATCA	11.0 h	0.8 ± 0.8	30 ± 7	5.5
				20 ± 6	9.0
				30 ± 6	7.25
298	ATCA	11.0 h	-0.3 ± 1.0	25 ± 7	5.5
				29 ± 6	9.0
				28 ± 6	7.25
320	ATCA	11.5 h	0.4 ± 0.8	27 ± 8	5.5
				22 ± 6	9.0
				22 ± 5	7.25
359	ATCA	9.5 h	–	<26	5.5
				<20	9.0
				<18	7.25
391	ATCA	9.5 h	–	<33	5.5
				<27	9.0
				<24	7.25
359	*Chandra*	67.2 ks	0.8 ± 0.4	$2.8^{+0.3}_{-0.5} \times 10^{-4}$	1.2×10^9
			0.585	$2.1^{+0.2}_{-0.3} \times 10^{-4}$	1.2×10^9

[a]X-ray fluxes are corrected for Galactic absorption along the sightlines.

(Troja et al. 2017) and a cocoon with energy injection (Mooley et al. 2018a), characterized by a *radial* profile of ejecta velocities. In Troja et al. (2018b) we developed semi-analytical models for both the structured jet and the quasi-spherical cocoon with energy injection, and showed that they describe the broad-band afterglow evolution during the first 6 months (from the afterglow onset to its peak) equally well. This is confirmed by numerical simulations of relativistic jets (Lazzati et al. 2018; Xie, Zrake & MacFadyen 2018) and choked jets (Nakar et al. 2018).

Several tests were discussed to distinguish between these two competing models (e.g. Gill & Granot 2018; Nakar et al. 2018). Corsi et al. (2018) used the afterglow polarization to probe the outflow geometry (collimated versus nearly isotropic), but the results were not constraining. Ghirlanda et al. (2019) and Mooley et al. (2018b) used very long baseline interferometry (VLBI) to image the radio counterpart, and concluded that the compact source size ($\lesssim 2$ mas) and its apparent superluminal motion favour the emergence of a relativistic jet core. A third and independent way to probe the outflow structure is to follow its late-time temporal evolution. In the case of a cocoon-dominated emission, the afterglow had been predicted to follow a shallow decay ($t^{-\alpha}$) with $\alpha \sim 1.0$–1.2 (Troja et al. 2018b) for a quasi-spherical outflow, and $\alpha \sim 1.35$ for a wide-angled cocoon (Lamb, Mandel & Resmi 2018). A relativistic jet is instead expected to resemble a standard on-axis explosion at late times, thus displaying a post-jet-break decay of $\alpha \sim 2.5$ (van Eerten & MacFadyen 2013).

Here, we present the results of our year-long observing campaign of GW 170817, carried out with the Australian Telescope Compact Array (ATCA) in the radio, *Hubble Space Telescope* (*HST*) in the optical, and the *Chandra X-ray Telescope* and *XMM–Newton* in the X-rays. Our latest observations show no signs of spectral evolution (Section 2.1) and a rapid decline of the afterglow emission (Section 2.2), systematically faster than cocoon-dominated/choked jet models from the literature (Section 3.1). The rich broad-band data set allows us to tightly constrain the afterglow parameters, and to compare the explosion properties of GW 170817 to canonical short GRBs (Section 3.2).
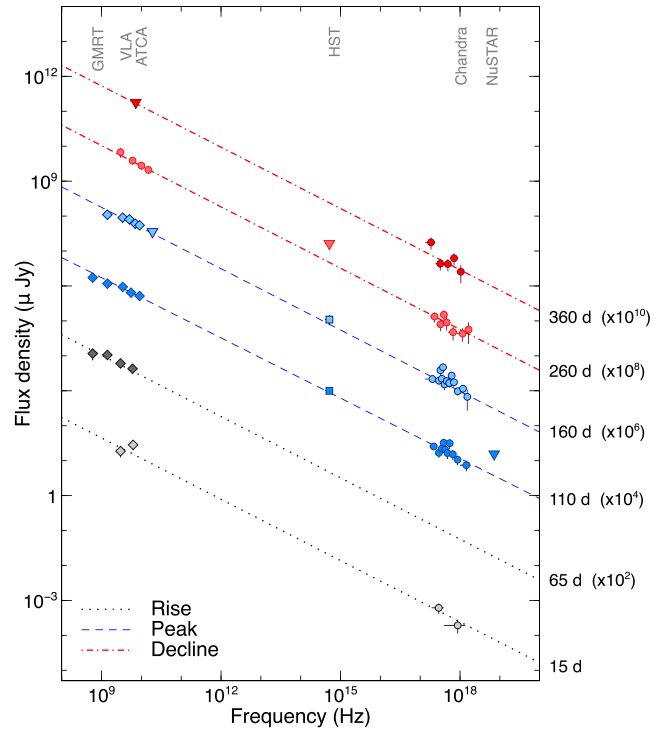
Figure 1. Temporal evolution of the afterglow spectral energy distribution. A single power-law segment can describe the broad-band spectrum during the different afterglow phases (rise, peak, and decline). At all times, a simple power-law model provides a good fit of the data.

2 OBSERVATIONS AND DATA ANALYSIS

Our earlier observations were presented in Troja et al. (2017, 2018b) and Piro et al. (2019). To these, we add a new series of observations tracking the post-peak afterglow evolution. Table 1 lists the latest unpublished data set, including our radio monitoring with ATCA (PI: Piro, Murphy) and X-ray observations with *Chandra*, carried out under our approved General Observer program (20500691; PI: Troja). Data were reduced and analysed as detailed in Troja et al. (2018b) and Piro et al. (2019). In the latest *Chandra* observation, the source is detected at a count rate of $(4.9 \pm 0.9) \times 10^{-4}$ counts s^{-1} in the 0.3–8.0 keV band, corresponding to an unabsorbed flux of $(6.70 \pm 0.13) \times 10^{-15}$ erg cm^{-2} s^{-1}. We adopted a standard Λ cold dark matter (ΛCDM) cosmology (Planck Collaboration VI 2018). Unless otherwise stated, the quoted errors are at the 68 per cent confidence level, and upper limits are at the 3σ confidence level.

2.1 Spectral properties

The latest epoch of X-ray observations shows a simple power-law spectrum with index $\beta = 0.8 \pm 0.4$, consistent with previous measurements, and with the spectral index 0.4 ± 0.3 from the late time ($t > 220$ d) radio data. Fig. 1 shows that, at all epochs, the broad-band spectrum can be fit with a simple power-law model with spectral index $\beta = 0.585 \pm 0.005$ and no intrinsic absorption in addition to the Galactic value $N_H = 7.6 \times 10^{20}$ cm^{-2}. The lack of any significant spectral variation on such long time-scales is remarkable. In GRB afterglows, a steepening of the X-ray spectrum due to the gradual decrease of the cooling frequency ν_c is commonly detected within a few days. Since the cooling break is a smooth spectral feature, we used a curved afterglow spectrum (Granot &
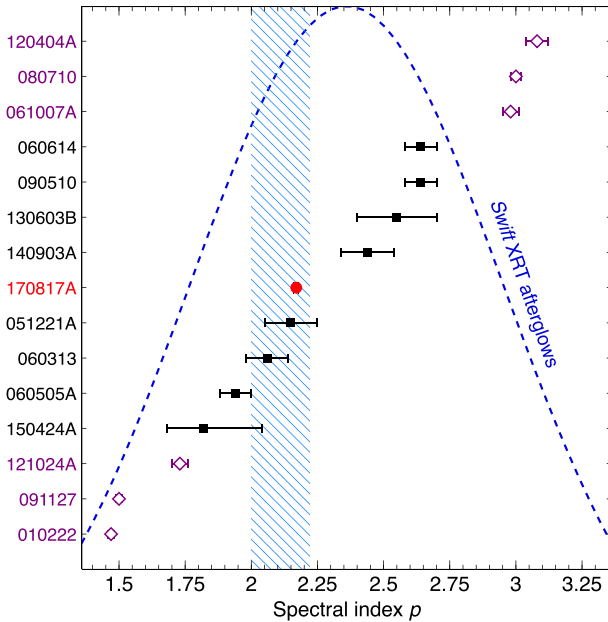
Figure 2. Spectral index p of the shock-accelerated electrons for GW 170817/GRB 170817A (filled circle) and a sample of short GRBs (filled squares) and long GRBs (open diamonds) with good afterglow constraints. The dashed line shows the distribution inferred from X-Ray Telescope (XRT) afterglows (Curran et al. 2010). The hatched area shows the range of values predicted by shock theory. Data are from Roming et al. (2006), Soderberg et al. (2006), Mundell et al. (2007), Resmi & Bhattacharya (2008), Xu et al. (2009), Krühler et al. (2009), Kumar & Barniol Duran (2010), Troja et al. (2012, 2016), Fong et al. (2015), Varela et al. (2016), and Knust et al. (2017).

Sari 2002) to fit the data, and constrain its location.[1] We derived $\nu_c \gtrsim 1$ keV (90 per cent confidence level) at 260 d after the merger and $\nu_c \gtrsim 0.1$ keV (90 per cent confidence level) at 360 d.

For a synchrotron spectrum with $\nu_m < \nu_{obs} < \nu_c$, the measured spectral index is related to the spectral index p of the emitting electrons (e.g. Granot & Sari 2002) as $p = 2\beta + 1 = 2.170 \pm 0.010$. Fig. 2 compares this value with a sample of well-constrained short and long GRB spectra. It shows that, among short GRB spectra, GW 170817/GRB 170817A represents the most precise measurement obtained so far. Such precision is rare, but not unprecedented among long GRB afterglows.

It is tempting to interpret the accurately determined value of p as an intermediate between relativistic and non-relativistic shock acceleration, based on theoretical considerations of plausible mechanisms (Kirk et al. 2000; Achterberg et al. 2001; Spitkovsky 2008), implying $\Gamma \approx 2$–10 for the emitting material (Margutti et al. 2018). On the other hand, various well-constrained short GRB p-values lie outside this theoretical range (Fig. 2), the p-value distribution for the larger sample of (long) GRBs does not appear consistent with a universal value for p (Shen, Kumar & Robinson 2006; Curran et al. 2010), nor is there generally any evidence for evolution of p from multi-epoch spectral energy distributions (SEDs; Fig. 1, also see Varela et al. 2016) or light-curve slopes. In view of these features of the general sample of long and short GRBs (as well as other synchrotron sources, such as blazars), direct interpretation

[1]The spectrum was fit with a curved spectrum leaving the cooling frequency as a free parameter. The best-fitting statistics C_0 was recorded, then the location of ν_c was changed until the variation in the fit statistics was equal to $C_0 + 2.706$.
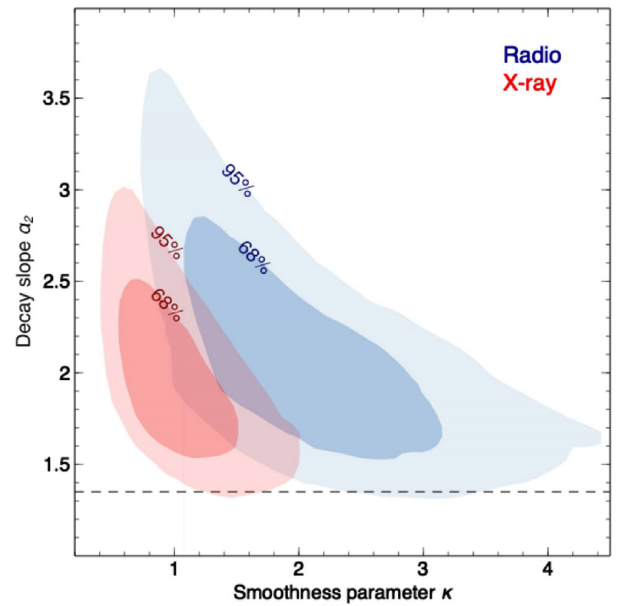

Figure 3. Joint marginal distribution of the decay index (α_2) and smoothness parameter (s) for the radio (blue) and X-ray (red) light curves. The dashed line corresponds to $\alpha_2 = 1.35$, the steepest value predicted by choked jet/cocoon models.

of $p \approx 2.17$ in terms of shock-acceleration theory might be premature.

2.2 Temporal properties

We simultaneously fit the multicolour (X-ray, optical, radio) light curves by adopting a simple power-law function in the spectral domain, and a smoothly broken power law in the temporal domain (Beuermann et al. 1999). The functional form is $F(\nu, t) \propto \nu^{-\beta} \left[(t/t_p)^{-\kappa\alpha_1} + (t/t_p)^{\kappa\alpha_2} \right]^{-1/\kappa}$, where β is the spectral index, α_1 and α_2 are the rise and decay slopes, t_p is the peak time, and κ is the smoothness parameter.

We did not impose an achromatic behaviour. Instead, the temporal properties were modelled as a hierarchy where the parameters for each wavelength have an independent value, sampled from a hyperdistribution. Variations in the hierarchy would be integrated out of the posterior if justified by the data.

Scale-family distributions were given lognormal priors and all other parameters were given normal priors. To fit the model, we employ the No-U-Turn Sampler (NUTS) variant of Hamiltonian Monte Carlo via the STAN modelling language (Carpenter et al. 2017). The peak time and rise slope are well constrained to $t_p = 164 \pm 12$ d and $\alpha_1 = 0.90 \pm 0.06$. Whereas the optical afterglow is poorly sampled, the X-ray and radio light curves allow for better constraints on the decay slope, $\alpha_2 = 2.0^{+0.8}_{-0.5}$ (Fig. 3), and are both consistent with a rapid decline of the afterglow flux. The best-fitting model and full corner plot are reported in the Supplementary Material (Fig. S1).

2.3 Modelling

We directly fit two semi-analytical models for structured outflows to the data, following the description in Troja et al. (2018b). The off-axis structured jet model assumes a Gaussian energy profile $E \propto \exp\left(-\theta^2/2\theta_c^2\right)$ up to a truncating angle θ_w. The

Table 2. Constraints on the Gaussian jet and Cocoon model parameters. Reported are the median values of each parameter's posterior distribution with symmetric 68 per cent uncertainties (i.e. the 16 and 84 per cent quantiles). The first Gaussian jet column uses constraints from the afterglow alone, the second includes the LIGO constraints on the inclination angle using the Planck value of H_0.

Parameter	Jet	Jet + GW + Planck	Parameter	Cocoon
θ_v	$0.52^{+0.16}_{-0.16}$	$0.38^{+0.11}_{-0.11}$	$\log_{10}u_{max}$	$1.38^{+0.92}_{-0.6}$
$\log_{10}E_0$	$52.47^{+0.81}_{-0.56}$	$52.80^{+0.89}_{-0.65}$	$\log_{10}u_{min}$	$0.51^{+0.36}_{-0.29}$
θ_c	$0.079^{+0.026}_{-0.024}$	$0.059^{+0.017}_{-0.017}$	$\log_{10}E_{inj}$	$56.1^{+3.2}_{-2.9}$
θ_w	$0.77^{+0.47}_{-0.38}$	$0.61^{+0.42}_{-0.31}$	k	$7.26^{+0.41}_{-0.57}$
			$\log_{10}M_{ej}$	$-8.2^{2.0}_{-1.3}$
$\log_{10}n$	$-1.83^{+0.77}_{-1.0}$	$-2.51^{+0.90}_{-0.99}$	$\log_{10}n$	$-4.5^{+2.1}_{-2.4}$
p	$2.1678^{+0.0064}_{-0.010}$	$2.1681^{+0.0062}_{-0.0095}$	p	$2.1715^{+0.0055}_{-0.0057}$
$\log_{10}\epsilon_e$	$-1.13^{+0.53}_{-0.88}$	$-1.39^{+0.62}_{-0.99}$	$\log_{10}\epsilon_e$	$-2.0^{+1.3}_{-1.3}$
$\log_{10}\epsilon_B$	$-4.18^{+0.85}_{-0.58}$	$-4.00^{+1.0}_{-0.69}$	$\log_{10}\epsilon_B$	$-3.4^{+1.7}_{-1.1}$
$\log_{10}E_{tot}$	$50.24^{+0.72}_{-0.47}$	$50.30^{+0.84}_{-0.57}$	$\log_{10}E_{tot}$	$52.4^{+1.2}_{-1.3}$

jet is fully determined by a set of eight parameters $\Theta_{jet} = \{E_0, n, \epsilon_e, \epsilon_B\ p, \theta_c, \theta_w, \theta_v\}$, where E_0 is the on-axis isotropic-equivalent kinetic energy of the blast wave, n the circumburst density, ϵ_e the electron energy fraction, ϵ_B the magnetic energy fraction, and θ_v the angle between the jet-axis and the observer's line of sight. Following Mooley et al. (2018a), we also fit a cocoon model with a velocity stratification of the ejecta to allow for a slower rise and late turnover. The total amount of energy in the slower ejecta above a particular four-velocity u is modelled as a power law $E(> u) = E_{inj}u^{-k}$. This model requires nine parameters $\Theta_{cocoon} = \{E_{inj}, n, p, \epsilon_e, \epsilon_B\ M_{ej}, u_{max}, u_{min}, k\}$, where u_{max} is the maximum ejecta four-velocity, u_{min} the minimum ejecta four-velocity, and M_{ej} the initial cocoon ejecta mass with speed u_{max}.

As described in Troja et al. (2018b), our Bayesian fit procedure utilizes the EMCEE Markov chain Monte Carlo package (Foreman-Mackey et al. 2013). For the structured jet we also include the GW constraints on the orientation ι of the system (Abbott et al. 2017a) in our prior for θ_v. The results of the MCMC analysis are summarized in Table 2. The best-fitting jet models are shown in Fig. 4. For the corner plot see the Supplementary Data (Fig. S2).
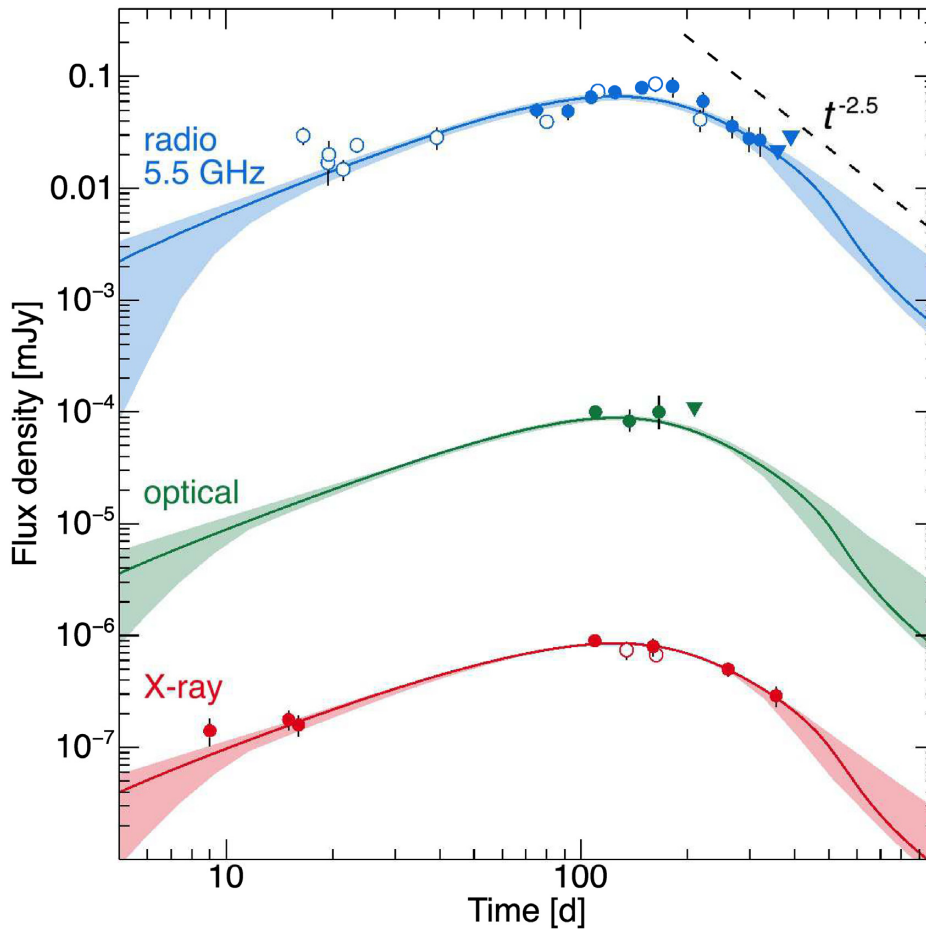

Figure 4. Multiwavelength afterglow light curves overlaid with the Gaussian jet best-fitting model (solid line) and its 68 per cent uncertainty range (shaded areas). Radio data are from ATCA (filled symbols) and Very Large Array (VLA, open symbols) observations. X-ray data are from *Chandra* (filled symbols) and *XMM–Newton* (open symbols) observations. Downward triangles are 3σ upper limits. The dashed line shows the expected asymptotic decline $\propto t^{-2.5}$. Data were collected from Troja et al. (2017, 2018b), Piro et al. (2019), Hallinan et al. (2017), Lyman et al. (2018), Resmi et al. (2018), Margutti et al. (2018), Mooley et al. (2018a), and Alexander et al. (2018).
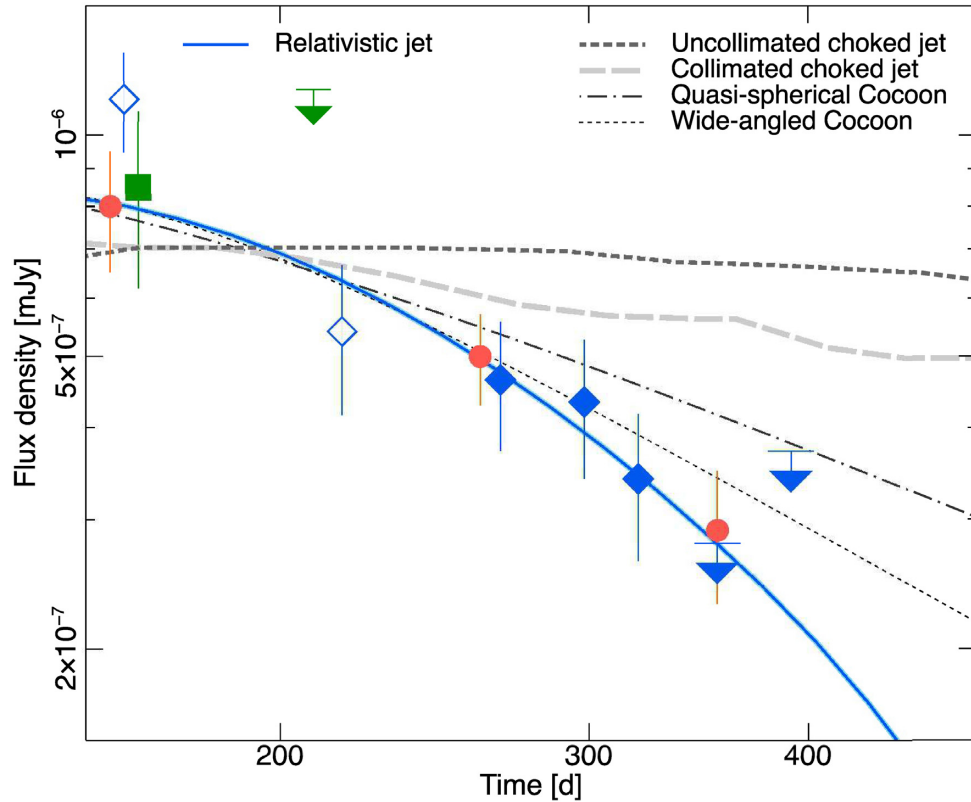
Figure 5. Late-time afterglow light curves compared to different explosion models: choked jets from numerical simulations (thicker lines; Nakar et al. 2018), wide-angled cocoon (Lamb et al. 2018), and our best-fitting models of quasi-spherical cocoon (dot–dashed line) and structured jet (solid line). Different symbols represent different wavelengths: X-rays (circles), optical (downward triangles; 3σ upper limits), and radio (diamonds) from ATCA (filled) and VLA (empty). For plotting purposes, data were rescaled to a common energy of 5 keV using the observed spectral slope $\beta = 0.585$.

3 RESULTS

3.1 A rapid afterglow decline: constraints on the outflow structure

For jets that fail to break out ('choked jets'), the jet energy is dissipated into a surrounding cocoon of material. This scenario is therefore included in our group of 'cocoon' models (Troja et al. 2018b). The post-peak temporal slope is a shallow decay of $\alpha \approx 1.0$–1.2 up to at least 300 d for GRB 170817A, as can be inferred from semi-analytical modelling of the evolution of a trans-relativistic shell (Troja et al. 2018b). Any remaining post-turnover impact due to continued energy injection from e.g. a complex velocity profile of the ejecta would lead to an even shallower decay. Afterwards, the slope will eventually become that of an expanding non-relativistic (quasi-)spherical shell. As for the Sedov–Taylor solution of a point explosion in a homogeneous medium, this slope translates to $\alpha = (15p - 21)/10$ for $\nu_m < \nu_{obs} < \nu_c$, when combined with a standard synchrotron model for shock-accelerated electrons (Frail, Waxman & Kulkarni 2000). The value $p \approx 2.17$ implies $\alpha \approx 1.155$. If $\nu_m, \nu_c < \nu_{obs}$, $\alpha = (3p - 4)/2 \approx 1.255$ instead (e. g. Granot & Sari 2002). If the cocoon choking the jet is not quasi-spherical, but merely wide angled, some sideways spreading of the outflow may still occur. By definition for a non-relativistic flow velocity, this will not produce any observational features related to relativistic beaming, but the continuous increase in working surface will give rise to additional deceleration of the blast wave relative to the case of purely radial flow. As a result, the temporal slope could steepen slightly by another $\Delta\alpha \approx 0.15 - 0.2$ (Lamb et al. 2018), before

settling into the late quasi-spherical stage. For GW 170817, this implies a maximum $\alpha \approx 1.35$ from a cocoon-dominated/choked jet model.

By contrast, if the jet has a relativistically moving inner region (in terms of angular distribution of Lorentz factor), the post-peak temporal slope will be like that of an on-axis jet seen after the jet break: the entire surface of the jet has come into view and there is no longer a contribution to the light-curve slope from a growing visible patch. Different calculations predict various degrees of steepening (e.g. Gill & Granot 2018): a slope $\alpha \approx p$ according to analytical models (Sari, Piran & Halpern 1999), and a somewhat steeper $\alpha \approx 2.5$ according to semi-analytical models (Troja et al. 2018b) and hydrodynamical simulations of jets (van Eerten & MacFadyen 2013, although the latter were done for jets starting from top-hat initial conditions).

As derived in Section 2.2, the decay slope α_2 of the empirical model exceeds the predictions of most choked jet models by a healthy margin. This is confirmed by the comparison of the late afterglow data, from radio to X-rays, with physical models of choked and structured jets (Fig. 5). The observed decay is consistent with the turnover of a structured jet (solid line). While the observed α_2 is not as steep as 2.5, this is not unexpected for a jetted flow as the transition of the light curve from rise to decay is spread out over time (and fully captured by the direct application of a structured jet model in Section 2.3, see also Fig. 4).

The rapid decline of the afterglow therefore poses an additional challenge to the choked jet models, in support to the results of the high-resolution radio imaging (Mooley et al. 2018b; Ghirlanda
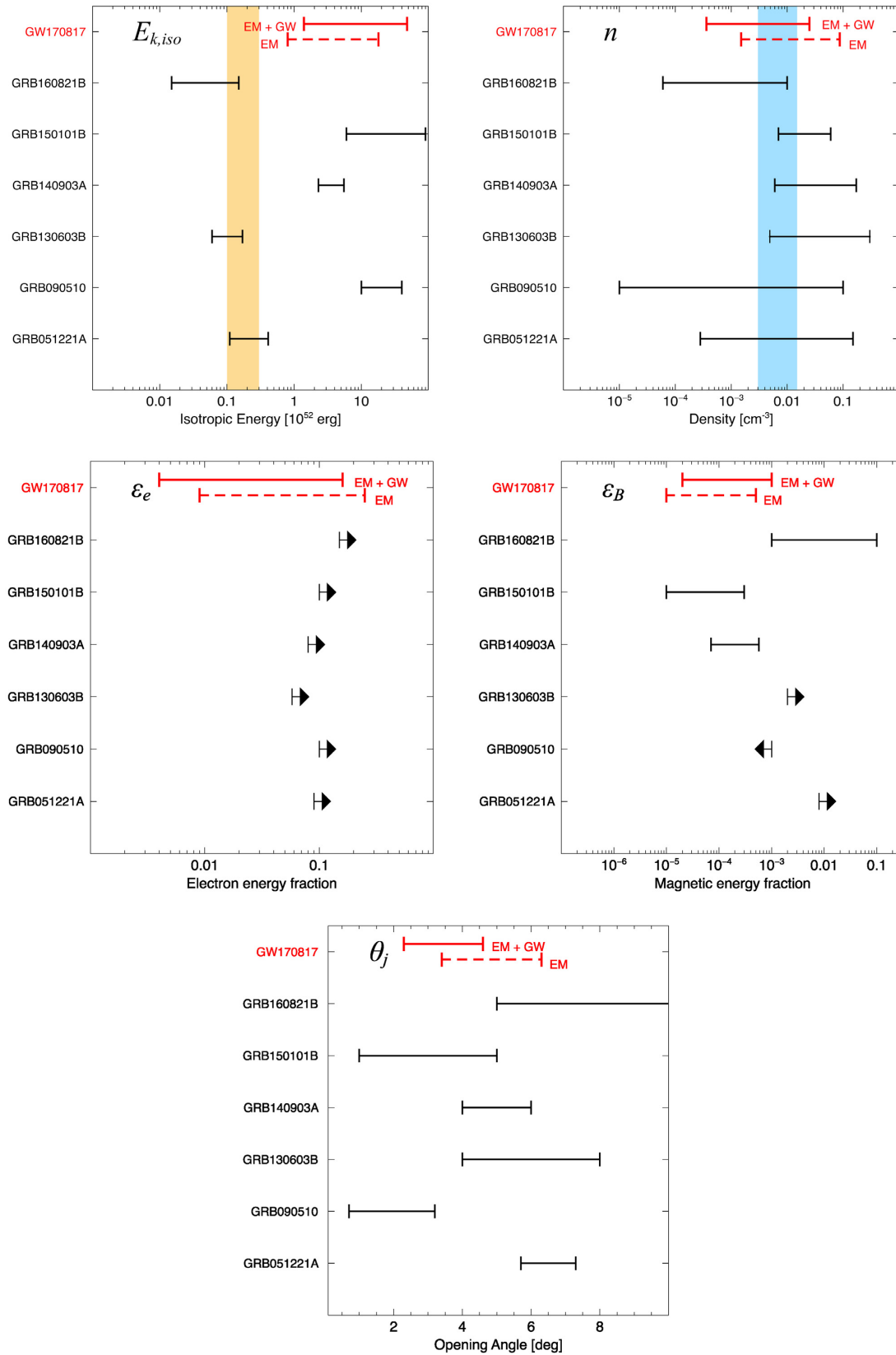
Figure 6. Afterglow parameters for GW 170817 and a sample of cosmological ($z > 0.1$) short GRBs with multiwavelength afterglows. For GW 170817 we report the results based purely on the electromagnetic observations (EM), and those incorporating the LIGO constraints on the binary inclination (EM + GW). Data are from Soderberg et al. (2006), Kumar & Barniol Duran (2010), Fong et al. (2015), and Troja et al. (2016, 2018a, 2019). The vertical grey band shows the median values of energy $E_{\rm k,iso}$ and density n for the larger sample of *Swift* short GRBs (Fong et al. 2015).

et al. 2019). While growing evidence indicates that the merger remnant launched a successful relativistic jet, the presence of a cocoon cannot be excluded. There might well be an observable cocoon component present in the outflow even for successful jets (Murguia-Berthier et al. 2014; Nagakura et al. 2014). Indeed, the structured jet itself might be an indication of the presence of a cocoon (in case the structure is not imposed by the torus upon launching; Aloy, Janka & Müller 2005). However, it would appear any such cocoon is not the dominant emission component at late times.

3.2 Afterglow properties: comparison to short GRBs

The predictive power of each model can be judged by the deviance information criteria (DIC), where lower scores correspond to greater predictive power (Spiegelhalter et al. 2002). The Gaussian jet model fit has a DIC of 103.5 and the cocoon model fit has a DIC of 151.8, favouring the Gaussian jet as the more predictive model. For all models and priors, the posterior value of the electron power-law slope lies around $p = 2.170 \pm 0.010$, fully consistent with the value obtained by the spectral analysis (Section 2.1).

The cocoon model requires a small amount of relativistic ejecta with a substantial Lorentz factor $\Gamma_{max} \in [6.1, 200]$ (all ranges with 68 per cent confidence) followed by an energetic tail of slower ejecta with minimum Lorentz factor $\Gamma_{min} \in [1.9, 7.48]$. The high Lorentz factors are in tension with a choked-jet scenario, where the ejecta achieve only Newtonian velocity. The total energy, assuming a spherical blast wave, is rather high, between 10^{51} and 4×10^{53} erg. The circumburst density and shock microphysical parameters are very poorly constrained in this model.

The Gaussian jet (Fig. 4) has a well-constrained width $\theta_c = 0.06 \pm 0.02$ rad ($3°.4 \pm 1°.1$), and a total energy between 5×10^{49} and 1.4×10^{51} erg. The wide truncation angle is largely unconstrained. The ambient density n is constrained to be between 3×10^{-4} and 2.4×10^{-2} cm^{-3}. The microphysical parameters $\epsilon_e \in [4 \times 10^{-3}, 0.17]$ and $\epsilon_B \in [2.7 \times 10^{-5}, 10^{-3}]$ are only somewhat constrained by the model fit. The constraint $\nu_c > 1$ keV from the lack of spectral steepening drives the relatively small value for ϵ_B, as $\nu_c \propto \epsilon_B^{-3/2}$. These values were derived by assuming a jet with a Gaussian angular profile, yet they are in good agreement with other estimates based on different angular structures (e.g. Ghirlanda et al. 2019).

The viewing angle derived from the electromagnetic observations alone is 0.52 ± 0.16 rad ($30° \pm 9°$), consistent with the constraints from prompt emission (e.g. Abbott et al. 2017b; Bégué, Burgess & Greiner 2017) and optical and radio imaging (Mooley et al. 2018b; Ghirlanda et al. 2019; Lamb et al. 2019). By adding the GW constraints on the binary inclination ι to our modelling, we obtain $\theta_v = 0.38 \pm 0.11$ rad ($22° \pm 6°$), consistent with the LIGO estimates that informed the prior. The good agreement of the electromagnetic and GW constraints suggests that the relativistic jet was launched nearly perpendicularly to the orbital plane.

The year-long monitoring of GW 170817 significantly reduced the allowed parameter space of models, tightening the constraints on the afterglow properties. This allows for a comparison with other well-studied short GRB explosions, as presented in Fig. 6. It is remarkable how the properties of GW 170817 fit within the range of short GRB afterglows. The low circumburst densities $n \approx 0.01$ cm^{-3} are typical of the interstellar medium, and consistent with the location of these bursts within their galaxy light. The electron energy fraction seems well constrained to $\epsilon_e \gtrsim 0.1$, whereas ϵ_B tends to lower values $\lesssim 0.01$, and is only loosely constrained. The

narrow width of the Gaussian jet θ_c of GW 170817 is comparable to the half-opening angle θ_j inferred from top-hat jet models of short GRBs (e.g. Troja et al. 2016), suggesting that these GRB jets had narrow cores of similar size. The isotropic-equivalent energy is also consistent with the measurements from other short GRBs, although we note that most events in the sample lie above the median value of $E_{k, iso}$ (vertical band). This is not surprising as we selected the cases of well-sampled light curves with good afterglow constraints, thus creating a bias toward the brightest explosions.

4 CONCLUSIONS

The long-term afterglow monitoring of GW 170817 supports the earlier suggestions of a relativistic jet emerging from the merger remnant, and challenges the alternative scenarios of a choked jet. Whereas emission at early times (<160 d) came from the slower and less energetic lateral wings, the rapid post-peak decline suggests that emission from the narrow jet core has finally entered our line of sight. The overall properties of the explosion, as derived from the afterglow modelling, are consistent with the range of properties observed in short GRBs at cosmological distances, and suggest that we detected its electromagnetic emission thanks to a combination of moderate off-axis angle (θ_v–$\theta_c \approx 20°$) and intrinsic energy of the explosion.

REFERENCES

Abbott B. P. et al., 2017a, Nature, 551, 85
Abbott B. P. et al., 2017b, ApJ, 848, L13
Achterberg A., Gallant Y. A., Kirk J. G., Guthmann A. W., 2001, MNRAS, 328, 393
Alexander K. D. et al., 2018, ApJ, 863, L18
Aloy M. A., Janka H.-T., Müller E., 2005, A&A, 436, 273
Bégué D., Burgess J. M., Greiner J., 2017, ApJ, 851, L19
Beuermann K. et al., 1999, A&A, 352, L26
Carpenter B. et al., 2017, J. Stat. Software, 76, 1
Corsi A. et al., 2018, ApJ, 861, L10
Curran P. A., Evans P. A., de Pasquale M., Page M. J., van der Horst A. J., 2010, ApJ, 716, L135
D'Avanzo P. et al., 2018, A&A, 613, L1
Fong W., Berger E., Margutti R., Zauderer B. A., 2015, ApJ, 815, 102
Foreman-Mackey D., Hogg D. W., Lang D., Goodman J., 2013, PASP, 125, 306
Frail D. A., Waxman E., Kulkarni S. R., 2000, ApJ, 537, 191
Ghirlanda G. et al., 2019, Science, 363, 968
Gill R., Granot J., 2018, MNRAS, 478, 4128
Granot J., Sari R., 2002, ApJ, 568, 820
Haggard D., Nynka M., Ruan J. J., Kalogera V., Cenko S. B., Evans P., Kennea J. A., 2017, ApJ, 848, L25
Hallinan G. et al., 2017, Science, 358, 1579
Kasliwal M. M. et al., 2017, Science, 358, 1559
Kathirgamaraju A., Barniol Duran R., Giannios D., 2018, MNRAS, 473, L121

Kirk J. G., Guthmann A. W., Gallant Y. A., Achterberg A., 2000, ApJ, 542, 235

Knust F. et al., 2017, A&A, 607, A84

Krühler T. et al., 2009, A&A, 508, 593

Kumar P., Barniol Duran R., 2010, MNRAS, 409, 226

Lamb G. P., Mandel I., Resmi L., 2018, MNRAS, 481, 2581

Lamb G. P. et al., 2019, ApJ, 870, L15

Lazzati D., López-Cámara D., Cantiello M., Morsony B. J., Perna R., Workman J. C., 2017, ApJ, 848, L6

Lazzati D., Perna R., Morsony B. J., Lopez-Camara D., Cantiello M., Ciolfi R., Giacomazzo B., Workman J. C., 2018, Phys. Rev. Lett., 120, 241103

Lyman J. D. et al., 2018, Nat. Astron., 2, 751

Margutti R. et al., 2018, ApJ, 856, L18

Mooley K. P. et al., 2018a, Nature, 554, 207

Mooley K. P. et al., 2018b, Nature, 561, 355

Mundell C. G. et al., 2007, ApJ, 660, 489

Murguia-Berthier A., Montes G., Ramirez-Ruiz E., De Colle F., Lee W. H., 2014, ApJ, 788, L8

Nagakura H., Hotokezaka K., Sekiguchi Y., Shibata M., Ioka K., 2014, ApJ, 784, L28

Nakar E., Gottlieb O., Piran T., Kasliwal M. M., Hallinan G., 2018, ApJ, 867, 18

Piro L. et al., 2019, MNRAS, 483, 1912

Planck Collaboration VI, 2018, preprint (arXiv:1807.06209)

Resmi L., Bhattacharya D., 2008, MNRAS, 388, 144

Resmi L. et al., 2018, ApJ, 867, 57

Roming P. W. A. et al., 2006, ApJ, 651, 985

Sari R., Piran T., Halpern J. P., 1999, ApJ, 519, L17

Shen R., Kumar P., Robinson E. L., 2006, MNRAS, 371, 1441

Soderberg A. M. et al., 2006, ApJ, 650, 261

Spiegelhalter D. J., Best N. G., Carlin B. P., van der Linde A., 2002, J. R. Stat. Soc. Ser. B, 64, 583

Spitkovsky A., 2008, ApJ, 682, L5

Troja E. et al., 2012, ApJ, 761, 50

Troja E. et al., 2016, ApJ, 827, 102

Troja E. et al., 2017, Nature, 551, 71

Troja E. et al., 2018a, Nat. Commun., 9, 4089

Troja E. et al., 2018b, MNRAS, 478, L18

Troja E. et al., 2019, preprint (arXiv:1905.01290)

van Eerten H., MacFadyen A., 2013, ApJ, 767, 141

Varela K. et al., 2016, A&A, 589, A37

Xie X., Zrake J., MacFadyen A., 2018, ApJ, 863, 58

Xu D. et al., 2009, ApJ, 696, 971

SUPPORTING INFORMATION

Supplementary data are available at *MNRAS* online.

Figure S1. Corner plot for the empirical model described in Section 2.2.
Figure S2. Fit result for the Gaussian jet model.

Please note: Oxford University Press is not responsible for the content or functionality of any supporting materials supplied by the authors. Any queries (other than missing material) should be directed to the corresponding author for the article.

This paper has been typeset from a TEX/LATEX file prepared by the author.